Refining the 2018 $M_{\rm w}$ 7.5 Papua New Guinea Earthquake Fault-Slip Model Using Subpixel Offset

Jeng-Hann Chong^{1,2} and Mong-Han Huang^{*1}

ABSTRACT

The $M_{\rm w}$ 7.5 earthquake that struck central Papua New Guinea in 2018 was the largest event ever recorded in the region with modern seismic instruments. The ground motions associated with this event also triggered widespread landslides and affected more than 500,000 people. However, due to the absence of a local seismic and Global Positioning System network in the vicinity, the fault location, system, and slip distribution of this earthquake are not well documented. In this study, we use the subpixel offset method on the Copernicus Sentinel-1 Synthetic Aperture Radar (SAR) images to calculate the 3D coseismic displacement of the 2018 Papua New Guinea earthquake. The results show clear fault traces that suggest coseismic slip on the Mubi fault and the Mananda fault that triggered landslides that spread out in a more than 260 km2 region. Finite-source inversions based on the subpixel offset measurements show up to 4.1 and 6.5 m coseismic slip on the Mubi and Mananda faults, respectively. Despite higher data uncertainty (~0.4-0.8 m) of the subpixel offset data, synthetic resolution tests show resolvable slip above 8 km in depth. The lack of shallower slip on the west side of the Mananda fault could be due to an inflated geothermal gradient near the dormant volcano, Mount Sisa, as a slip barrier. The result of the coulomb stress change suggests possible southeastward slip propagation from the Mananda fault to the Mubi fault. Our work successfully resolves 3D coseismic displacement in highly vegetated terrains and demonstrates the feasibility of using the subpixel offset on SAR images to help our understanding of regional active tectonic systems.

KEY POINTS

- The subpixel offset method reveals the 2018 Papua New Guinea earthquake coseismic displacement in 3D.
- At least two faults located in different parts of the Papuan fold-and-thrust belt slipped in this event.
- This work shows the utility of the subpixel method for resolving displacement in highly vegetated terranes.

Supplemental Material

INTRODUCTION

Located in the southwest of the Pacific Ocean, Papua New Guinea is actively deforming due to the collision between the Australian plate and the Pacific plate with convergence rate of ~110 mm/yr (Tregoning *et al.*, 2000; Wallace *et al.*, 2004). On the 25th of February 2018, an $M_{\rm w}$ 7.5 earthquake occurred within the densely vegetated Papuan fold-and-thrust belt area (Fig. 1). This was the largest earthquake recorded in this region with modern seismic instruments. The U.S. Geological Survey

(USGS) National Earthquake Information Center (NEIC) focal mechanism recorded the epicenter at an \sim 25 km depth, and their finite-fault solution suggests coseismic slip on an eastwest strike thrust fault that is 210 km in length and 72 km in width. The mainshock was subsequently followed by at least 39 aftershocks of $M_{\rm w} > 4$ within 24 hr. Although the aftershock locations are not well determined, there is a general northwest–southeast trend that follows the orientation of the main fold-and-thrust structure (Fig. 1). The seismic moment constrained by the USGS uses teleseismic data, with the nearest station more than 600 km away from the hypocenter in Port Moresby, Papua New Guinea. Because of the lack of available data from regional Global Positioning System

Cite this article as Chong, J.-H., and M.-H. Huang (2020). Refining the 2018 $M_{\rm w}$ 7.5 Papua New Guinea Earthquake Fault-Slip Model Using Subpixel Offset, *Bull. Seismol. Soc. Am.* **111**, 1032–1042, doi: 10.1785/0120200250

© Seismological Society of America

^{1.} University of Maryland, College Park, Maryland, U.S.A.; 2. Now at California State University, Northridge, California, U.S.A.

^{*}Corresponding author: mhhuang@umd.edu

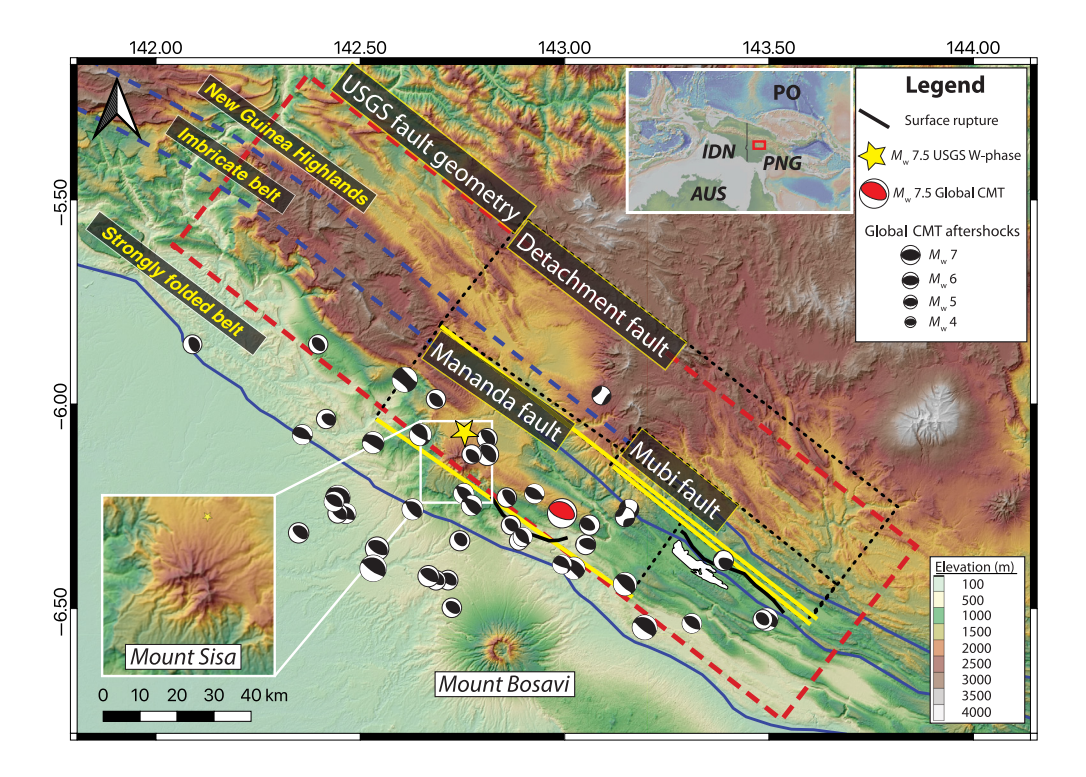


Figure 1. Digital elevation map of the studied region in the southern Highlands plotted with the U.S. Geological Survey (USGS) mainshock (yellow star) and Global Centroid Moment Tensor (Global CMT) mainshock (red focal mechanism plot). The black focal mechanism plots are two-month aftershocks with Global CMT moment tensor solutions. Yellow lines indicate the up-dip edge of the fault plane, and black lines show the fault traces shown in subpixel offsets (Fig. 3). The red box in the inset shows the study area. AUS, Australia; IDN, Indonesia; PO, Pacific Ocean; PNG, Papua New Guinea. The color version of this figure is available only in the electronic edition.

networks in the country, there are no in situ surface geodetic measurements of this event.

To gain a better understanding of this earthquake, Wang et al. (2020) used the L-band (wavelength \approx 24 cm) Advanced Land Observing Satellite-2 (ALOS-2) Interferometric Synthetic Aperture Radar (InSAR) to study the coseismic surface displacement and proposed a fault model that is composed of four fault segments to explain the InSAR measurements. Based on their inversion, the coseismic slip is up to 1.9 m, and slip extends down to an \approx 25 km depth. Their estimated coseismic moment is \approx 1.90 \times 10²⁰ N·m, equivalent to $M_{\rm w}$ 7.46. Although Wang et al. (2020) were able to retrieve most of the far-field coseismic displacement using the ALOS-2 InSAR, near-field displacement is not well resolved due to higher decorrelation and possible phase unwrapping errors.

The subpixel offset measures the surface movement between two amplitude images, and it has successfully constrained large surface displacement such as the 2010 $M_{\rm w}$ 7.2 El Mayor–Cucapah earthquake (Huang, Fielding, Dickinson, et al., 2017), the 2013 $M_{\rm w}$ 7.1 Bohol earthquake (Kobayashi, 2014), and the 2019 $M_{\rm w}$ 7.1 Ridgecrest earthquakes (Fielding et al., 2020; Milliner and Donnellan, 2020). The focus of this study is to measure the 2018 Papua New Guinea

earthquake coseismic deformation using the subpixel offset method on Synthetic Aperture Radar (SAR) images and to constrain the fault geometry as well as the fault slip based on the coseismic displacement measurements. The subpixel offset method allows us to detect reliable surface displacement within a densely forested region and to estimate fault geometry and slip fault distribution.

Geological setting of the Papuan fold-and-thrust belt

The New Guinea Highlands extends over a ~1300 km× ~150 km region across the central New Guinea Island (Baldwin et al., 2012; Fig. 1). The New Guinea Highlands has a relative displacement rate of ~13 mm/yr from the east side to ~6 mm/yr to the west with respect to the Australian plate (Koulali et al., 2015). The Papuan fold-and-thrust belt is

the southern end of the New Guinea Highlands. It also highlights the boundary between the New Guinea Highlands and the stable platform of the Australian plate to the south (Hamilton, 1979; Koulali *et al.*, 2015). In this article, we define the different sections of the Papuan fold-and-thrust belt based on the structural differences suggested by Hill *et al.* (2010) (Fig. 1). The hinterland is located toward the northeast, and the foreland is located toward the south–southwest. Detachment-involved thrusting is expected at the strongly folded belt and imbricate belt (Abers and McCaffrey, 1988).

DATA AND METHODSSubpixel offset

For SAR images, the subpixel offset (also known as pixel tracking) method calculates the offset of pixels between two amplitude images in the cross-track (range) and along-track (azimuth) directions. Although the result of the subpixel offset is not as precise as InSAR, it is widely used for measuring surface deformation when the offset is in meter scale, in which InSAR phase unwrapping errors may be significant, and/or when InSAR cannot provide reliable measurements due to low phase coherence, especially in regions with dense vegetation (e.g., Fialko *et al.*, 2001; Pathier *et al.*, 2006; Huang, Fielding,

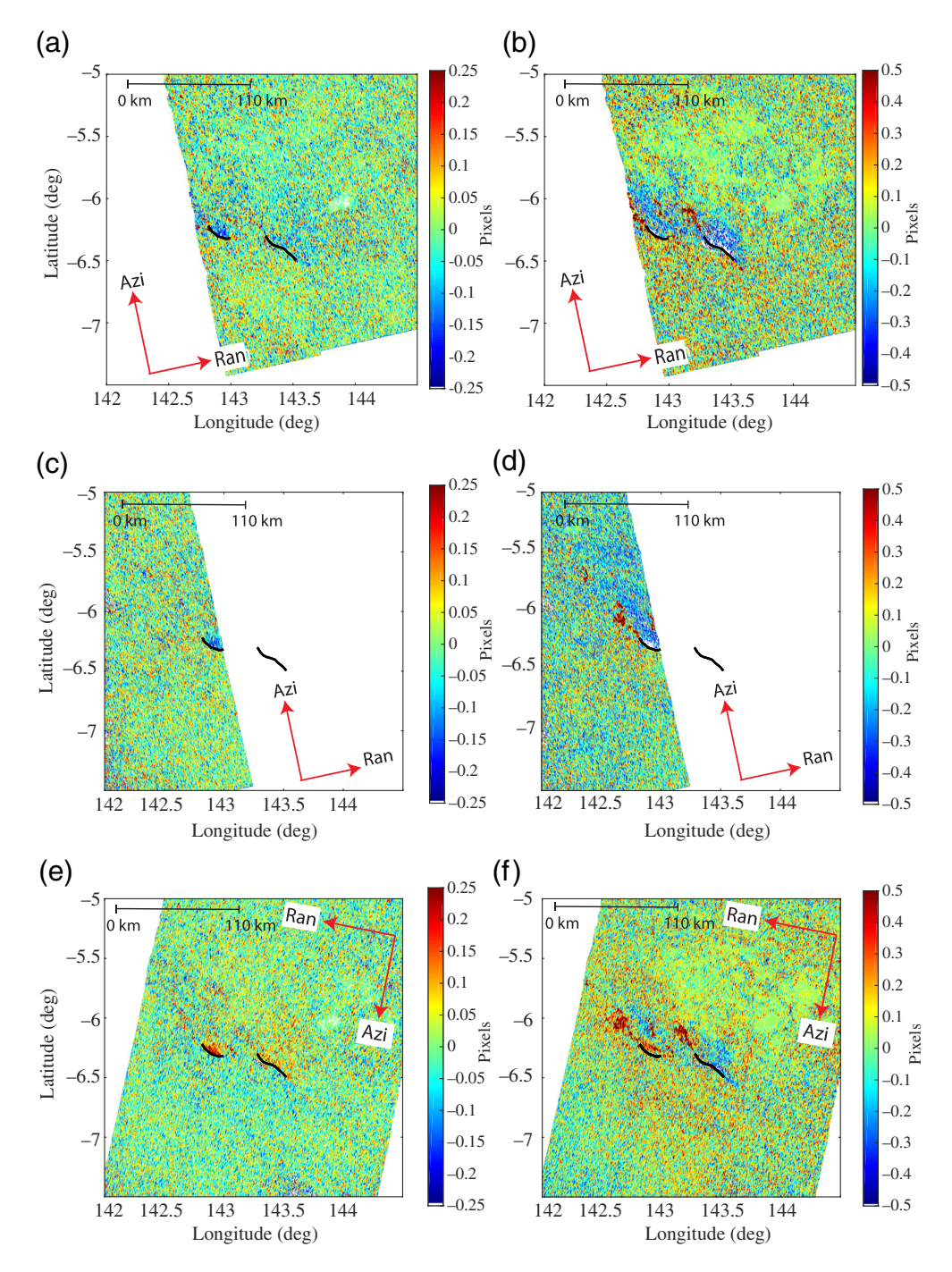


Figure 2. Azimuth (left) and range offset (right) of the ascending and descending tracks used in this study. Panels (a, b) represent ascending track A9; panels (c,d) represent ascending track A82; panels (e,f) represent descending track D133. The satellite heading direction is labeled as "Azi," and the line of sight of the satellite is labeled as "Ran." Note that the color scale is different for azimuth and range offset (unit in pixel). Black lines indicate the fault trace identified in this study. The color version of this figure is available only in the electronic edition.

Dickinson, *et al.*, 2017). In this study, we use the open-source software ISCE 2.3 (Rosen *et al.*, 2012) to process the Copernicus Sentinel-1 (S1) SAR single-look-complex scenes in the interferometric wide swath mode. We first select ascending or descending SAR image pairs that cross the 2018 earthquake, process each pair up to the interferometry level, and then use the

denseoffsets and filteroffsets modules to perform subpixel offset. During the subpixel offset process, an overlapping matching window with 64×64 pixels (~250 m in range and ~900 m in azimuth) in size is applied to the entire scene, with steps of 130 pixels in range and 21 pixels in azimuth (~300 m interval in the ground surface). After calculating the offset and georeferencing the offset product, we apply a median filter with a window size of 3×3 pixels to eliminate high-frequency noise.

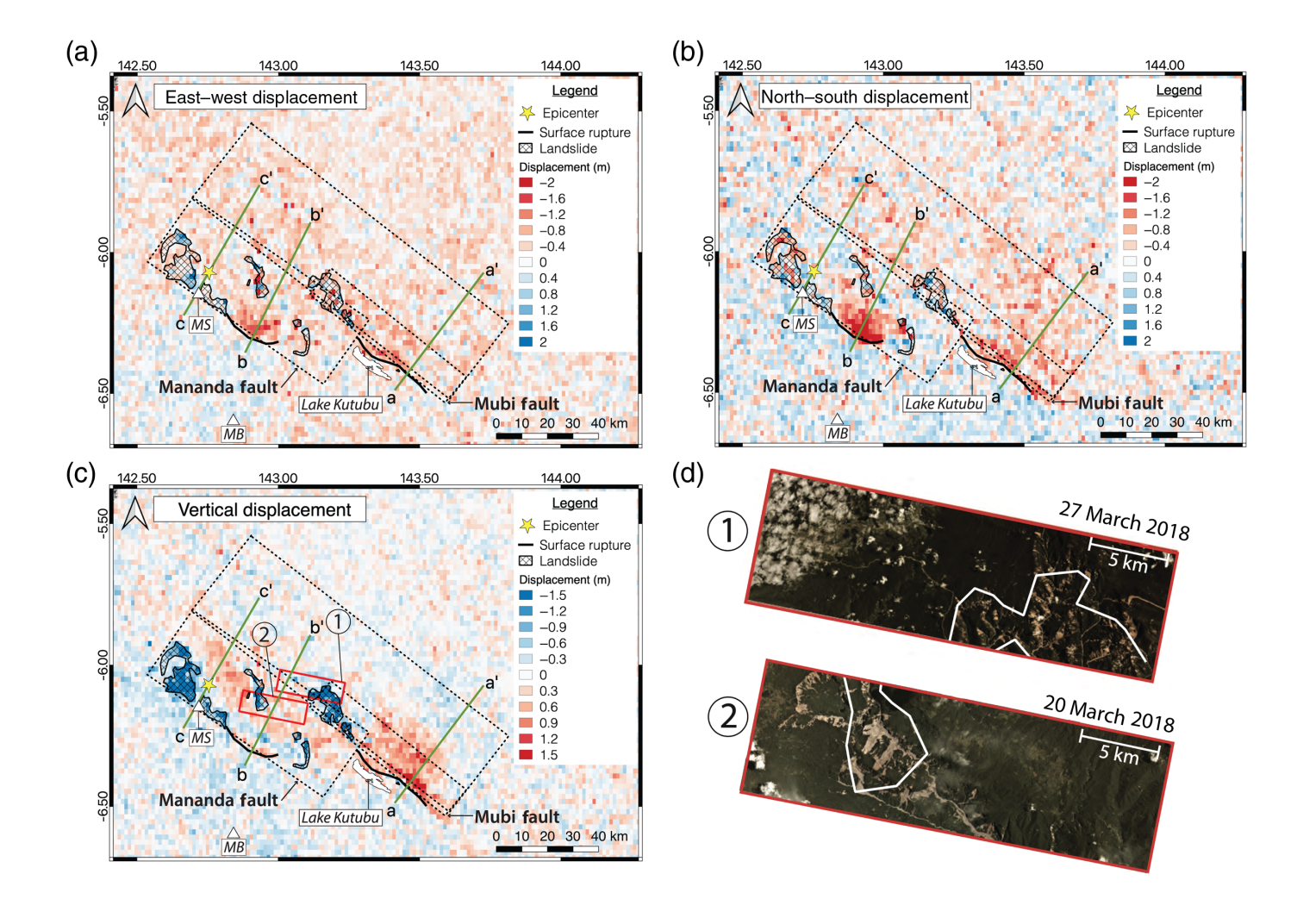
After performing the subpixel offset on two ascending and one descending coseismic S1 pairs, we obtain coseismic displacement in both the range and azimuth directions (Fig. 2 and Table 1). The displacement in the range direction (d_{RAN}) is written as

$$d_{\text{RAN}} = \cos \phi \sin \theta d_{\text{EW}}$$
$$+ \sin \phi \sin \theta d_{\text{NS}} - \cos \theta d_{\text{UD}},$$

in which $d_{\rm EW}$, $d_{\rm NS}$, and $d_{\rm UD}$ represent displacement in the east-west, north-south, vertical directions, respectively. Here, we assume the right-hand rule, so the satellite heading direction (ϕ) of the ascending and descending tracks is ~10° and ~170°, respectively. The satellite look angle (θ) of S1 is between 29° and 46°. The information of the S1 look direction and look angle of each pixel is from the rdr product in InSAR Scientific Computing Environment (ISCE). With the same notations, the displacement in azimuth (d_{AZI}) is written as

$$d_{\text{AZI}} = -\sin\phi d_{\text{EW}} + \cos\phi d_{\text{NS}}$$
.

Vertical displacement $(d_{\rm UD})$ does not contribute to displacement in azimuth $(d_{\rm AZI})$. Positive values in $d_{\rm RAN}$ and $d_{\rm AZI}$ represent increase of distance between the satellite and the ground surface.



Because the satellite heading direction (ϕ) and look angle (θ) are estimated by ISCE, the measured subpixel offset of ascending and descending tracks is then written in terms of 3D displacements (i.e., $d_{\rm EW}$, $d_{\rm NS}$, and $d_{\rm UD}$). In other words, the 3D displacements are estimated from the subpixel offset measurements in the range $(d_{\rm RAN})$ and azimuth $(d_{\rm AZI})$ directions of the ascending and descending tracks using linear inversions. We use least-squares inversions to constrain 3D displacement from the subpixel offset measurements. The entire study area is covered by one ascending and one descending track, so we estimate 3D displacement from at least four independent measurements (Figs. 2 and 3).

Figure 3. (a,b,c) 3D coseismic displacement of the region along with (d) Planet Labs optical images (see panel (c) for locations). The earth-quake-triggered landslides are identified with white polygons in panel (d) and black polygons with cross-hatch patterns in panels (a—c). In panels (a—c), fault traces are marked with black lines, and the yellow star is the USGS epicenter location. Warm colors indicate uplift, eastward, or southward displacement, and cold colors indicate subsidence, westward, or northward displacement. MB and MS represent Mount Bosavi and Mount Sisa, respectively. Green lines are transects shown in Figure 7. The color version of this figure is available only in the electronic edition.

TABLE 1		
Sentinel-1 (S1) Synthetic Aperture Radar Images Used in 1	ſhis	Study

Track	Primary (yyyy/mm/dd)	Secondary (yyyy/mm/dd)	Days Following the Earthquake
9 (ascending)	2018/02/23	2018/03/07	9
82 (ascending)	2018/02/16	2018/02/28	3
133 (descending)	2018/02/19	2018/03/03	6

The 25 February 2018 earthquake occurred between the primary and secondary image dates.

Finite-fault model

To determine the fault geometry that best describes the coseismic displacement, we perform a series of finite-fault inversions to determine first the fault geometry and then the fault slip. We determine the preferred fault geometry based on comparing the model misfits with different combinations of nominal fault parameters and then solve for the coseismic slip with the preferred fault geometry.

To begin, we generate a layered elastic structure from the CRUST1.0 velocity model (Laske et al., 2013) in the study area (6.5° S, 143.5° E; Table S1, available in the supplemental material to this article). The Green's functions are computed using the EDGRN/EDCMP code (Wang et al., 2003) with the source-toreceiver distance between 0 and 200 km and the source depth between 0 and 40 km. We construct two faults, the Mananda and Mubi faults, to explain the distribution of the coseismic displacement. The strike of each fault is determined by fitting the fault traces in the coseismic displacement. From seismic reflection work and structural geology mapping, Hill et al. (2010) and Keenan and Hill (2015) suggest a detachment connecting the down-dip extension of the two faults toward the New Guinea Highlands. We also include this proposed detachment in the modeling, with the depth of the detachment at 10 km and the dip angle at \sim 6° (Hill et al., 2010).

Each fault plane is composed of number of 2×2 km² subfaults. We use the non-negative least-squares method to invert for slip of each subfault with the given fault parameters, Green's function, and the coseismic displacement. We calculate the reduced chi-square (χ^2) misfit of each inversion and compare the χ^2 values between different assigned fault parameters. The reduced χ^2 is defined as

$$\chi^2 = \frac{1}{3N} \sum_{i=1}^{N} \left(\frac{d_{i_{\text{E,N,Z}}} - m_{i_{\text{E,N,Z}}}}{\sigma_{\text{E,N,Z}}} \right)^2$$
,

in which d_i , and m_i represent the ith observation and model, respectively. E, N, and Z represent the east–west, north–south, and vertical components, respectively. The uncertainty of the subpixel offset ($\sigma_{\rm E,N,Z}$) is estimated from a region without coseismic displacement (between 6.65–6.6° S and 142.4–142.6° E) and is explained further in the Results section. In general, a reduced χ^2 value close to 1 indicates model misfits equivalent to observational uncertainty.

We set the width of the Mananda fault and the Mubi fault as 40 km, and the fault length based on the spatial pattern of coseismic displacement of each fault. The initial dip angle of the two faults is 33° as determined from the USGS NEIC solution. To optimize the fault geometry, we vary the dip angle of one fault between 5° and 45° with 5° increment while keeping the dip angle of the other fault fixed. We repeat the same process to optimize the dip angle of the other fault. The dip angle of each fault is determined from the model that predicts the lowest reduced χ^2 value (Fig. 4).

After obtaining the preferred dip angles of each fault, we determine the smoothing parameter in the model. Similar to Huang *et al.* (2013), we vary the smoothing parameter for a few orders and select the highest smoothing value that can still predict a relatively low mean reduced χ^2 value of the three components (the thick black lines in Fig. 4). The last step in determining the fault geometry is to determine the rake of each fault. We assume a uniform rake for each fault and vary the rake of each fault between 70° and 110° while holding the other fault rake as 90°. Once we determine the rake of one fault, we repeat this process for the other fault. We did not vary the dip and rake angle of the detachment fault as the surface geodetic measurements could not constrain the fault geometry well (Fig. S2).

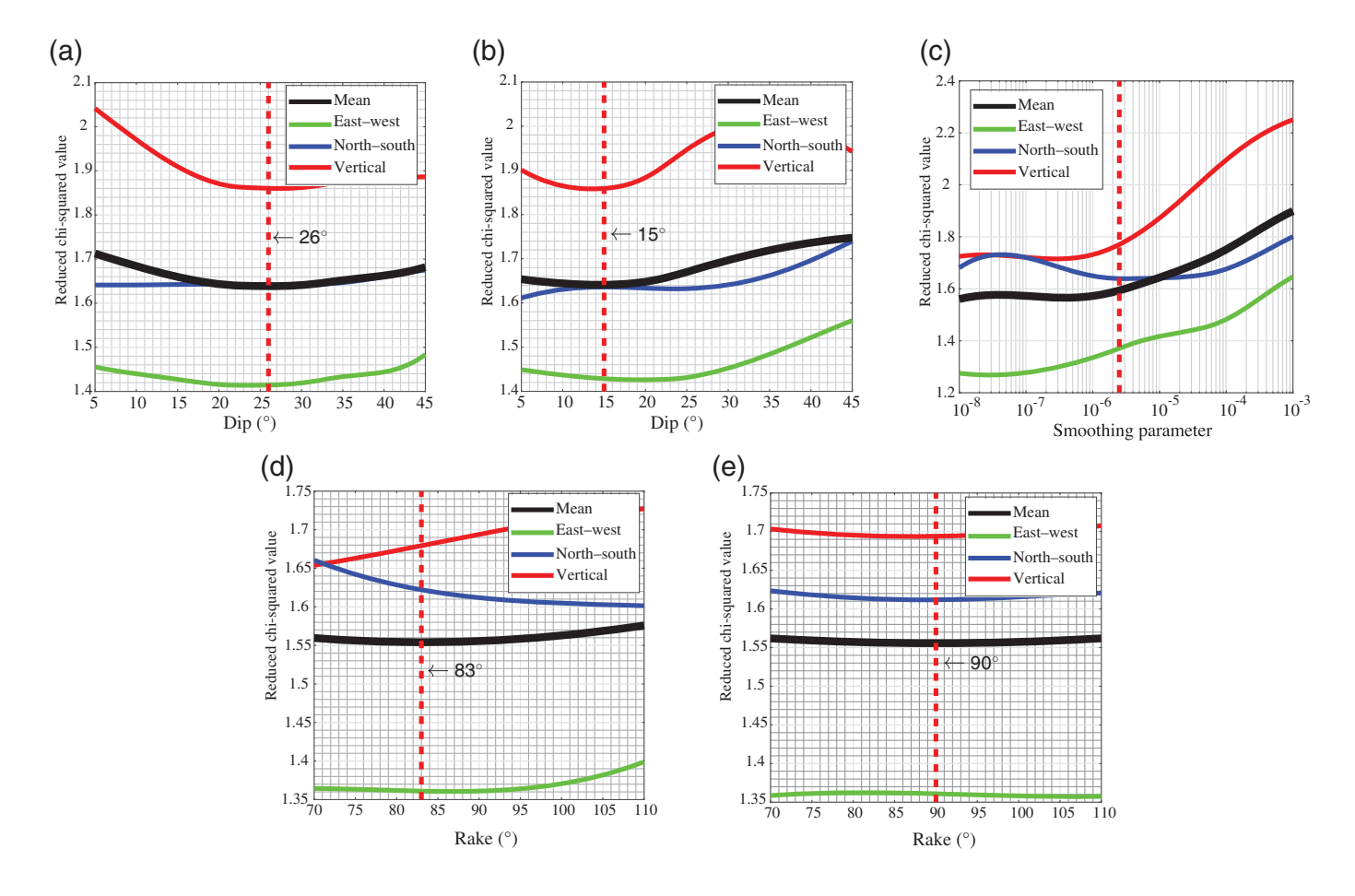
RESULTS

Subpixel offset displacement

We identified and traced two distinct high-surface-displacement regions from the sharp change of displacement in the vertical component (Fig. 3). The Mubi fault is located closer to the New Guinea Highlands, and the Mananda fault is located closer to the Mananda anticline in the frontal Papuan fold-and-thrust belt. The maximum vertical displacement near the Mubi fault is \sim 2 m, and that near the Mananda fault is \sim 1 m. The peak horizontal displacement generated by the Mubi and Mananda faults is 2.3 and 4.3 m, respectively. The coseismic displacement of the Mananda fault has a curved fault trace as opposed to the linear fault trace of the Mubi fault (Fig. 3).

The surface subsidence detected by the subpixel offset highlights the earthquake-triggered landslides as close as ~5 km away from the epicenter to more than 80 km away from the epicenter (Fig. 3c,d). Optical satellite mosaic imagery produced by the Planet Lab one month after the earthquake shows comparable locations and distributions of these earthquaketriggered landslides with our subpixel offset results. Although individual landslides are better recognized by the optical imagery, optical imagery fails to capture the full landslide distribution due to the presence of clouds. Our SAR subpixel offset measurement, on the other hand, is able to show an extensive, cloud-free distribution of landslides three days after the earthquake. Detailed analysis of the landslides is beyond the scope of this study, but we find that some of the triggered landslides are far away from the areas with higher coseismic displacements. This finding implies that these landslides were triggered by coseismic ground motion rather than static displacement. Nevertheless, to reduce bias due to fitting triggered landslides in slip inversion, we remove the subpixel offset results related to the triggered landslides prior to the finitefault inversions (black polygons in Fig. 3).

To evaluate the measurement uncertainty of subpixel offsets, we first assume that the uncertainty is spatially correlated, as is common in InSAR (e.g., fig. S3 in Huang, Fielding, Liang,



et al., 2017). By applying the method used in Bekaert et al. (2015), we calculate the covariogram of the subpixel offset measurement in three components with the earthquake-related displacement removed. The result shows a very low spatial noise correlation (<3 km) in each component (Fig. S1), so we consider the noise to not be clearly correlated in space. We then estimate the uncertainty of the subpixel offset $(\sigma_{E,N,Z})$ from calculating the standard deviation of the subpixel offsets in an area without coseismic displacement (between 6.65°-6.6° S and 142.4-142.6° E). The standard deviation for east-west, north-south, and vertical displacement is 31, 38, and 20 cm, respectively. Coseismic interferograms are also generated during the subpixel offset process in ISCE; however, they do not show a reliable deformation fringe pattern due to high-phase decorrelation of C-band (wavelength = \sim 5.6 cm) in densely vegetated regions (Fig. S1).

Figure 4. Reduced χ^2 analysis for the dip, rake, and smoothing parameters for the Mubi fault and the Mananda fault. (a) Dip analysis of the Mananda fault; (b) dip analysis of the Mubi fault; (c) smoothing parameter analysis; (d) rake analysis of the Mananda fault; and (e) analysis of the Mubi fault. Red, blue, and green curves represent the reduced χ^2 values of the vertical, north—south, and east—west components, respectively. The black curve is the mean reduced χ^2 of the three components. Red vertical dashed lines indicate the lowest reduced χ^2 mean value. The preferred fault parameters can be found in Table 2. The preferred smoothing parameter is 2.5×10^{-6} . The color version of this figure is available only in the electronic edition.

Finite-fault inversion

Following the Finite-Fault Model section, the inferred dip of the Mubi and Mananda faults is 26° and 15°, respectively (Fig. 4 and Table 2). The Mubi and Mananda faults are truncated by the detachment at a depth range between 8 and 10 km

TABLE 2
Preferred Fault Parameters for the Mubi Fault, the Mananda Fault, and the Detachment Fault

Fault Parameter	Mubi Fault	Mananda Fault	Detachment Fault
Strike, dip, and rake (°)	308, 26, and 90	305, 15, and 83	307, 6, and 90
Fault size (along strike and dip) (km)	70 and 22	86 and 32	130 and 40
Number of subfaults (horizontal and vertical)	35 and 11	43 and 16	65 and 20
Starting depth (km)	0.49	0.26	7.9

The subfault size is 2 km × 2 km.

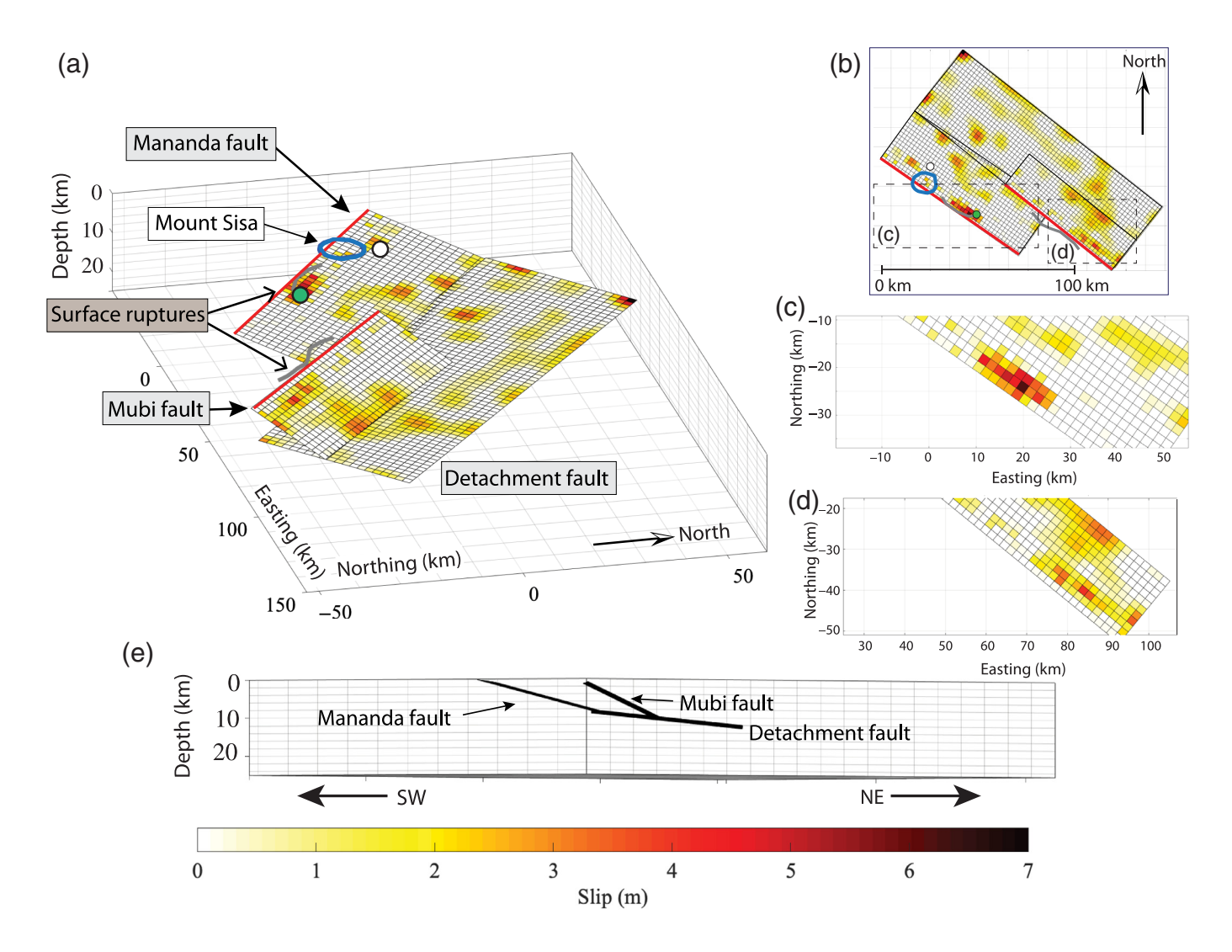


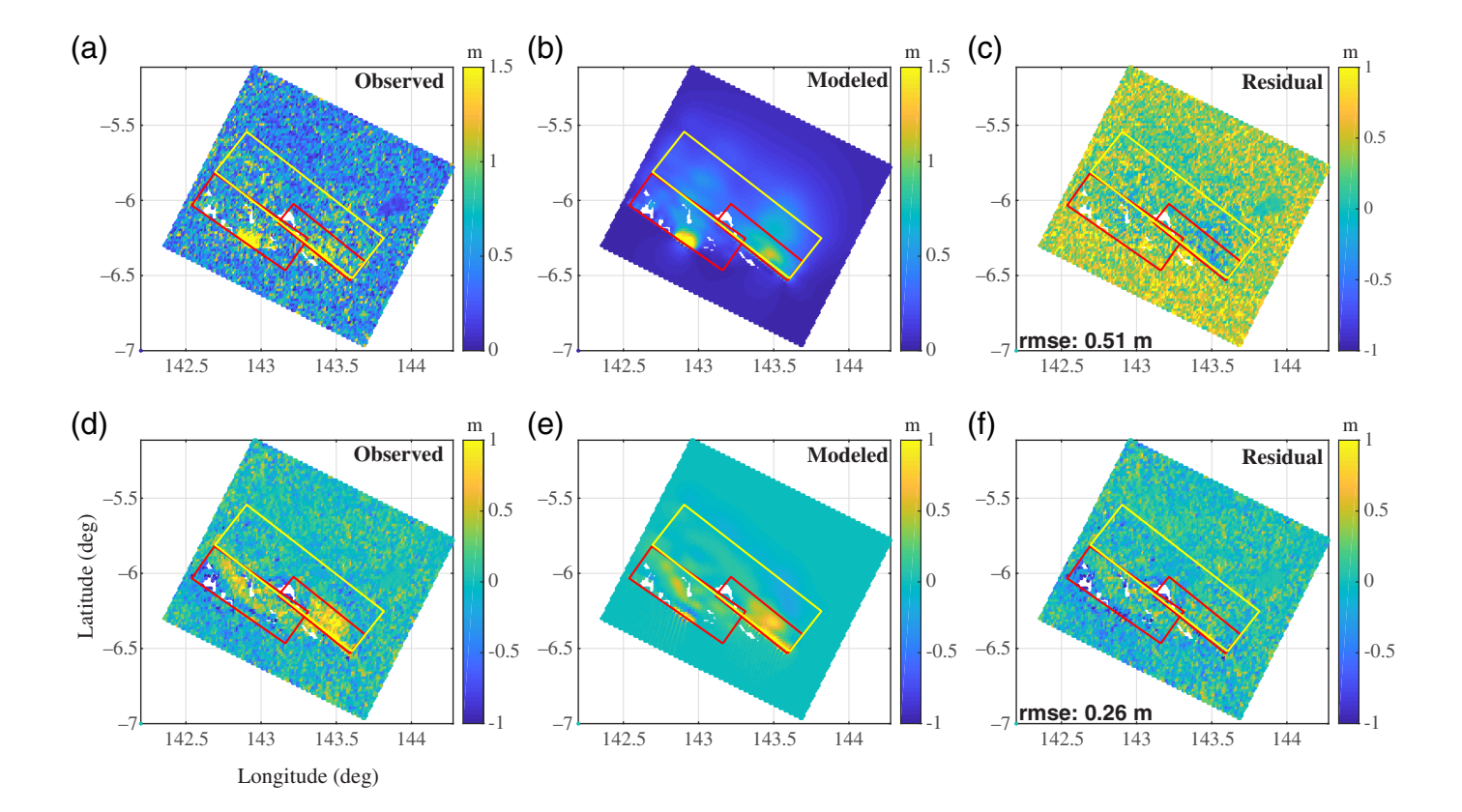
(Fig. 5). We vary the smoothing parameter between 10^{-8} and 10^{-2} and find a significant increase of reduced χ^2 when the smoothing is greater than 10^{-6} . We then determine the smoothing parameter as 2.5×10^{-6} to ensure a relatively smooth slip distribution that fits the data well (Fig. 4). The inferred rake is 90° and 83° for the Mubi and Mananda faults, respectively. Our inferred dip of the two faults is $\sim 10^{\circ} - 20^{\circ}$ shallower than the USGS NEIC solution (33°), and the inferred rakes are also lower than the NEIC solution (110°).

The peak slip of the Mubi fault and the Mananda fault is \sim 4.1 and \sim 6.5 m, respectively. The peak slip of the Mananda fault is shallower (less than 2 km in depth) than that of the Mubi fault (\sim 2–5 km in depth) (Fig. 5). The slip on the detachment is less than 3 m; however, as suggested in the checkerboard test (Fig. S3), the slip on the northwest corner of the detachment may not be reliable and is likely due to overfitting data noise at greater depth.

The estimated moment of the three faults is $\sim 1.51 \times 10^{20} \text{ N} \cdot \text{m}$ (M_{w} 7.42). Our modeled seismic moment is lower than the USGS NEIC solution (M_{w} 7.5), but it is similar to the estimation by Wang *et al.* (2020) (M_{w} 7.46) using ALOS-2 InSAR as constraints.

Figure 5. (a) 3D view, (b) top views, (e) and cross-section view of the fault model. Yellow-to-red colors indicate a greater amount of slip on the fault. Panels (c,d) highlight shallow slip of the Mananda and Mubi faults. The peak slip of the Mananda fault is less than \sim 2 km in depth, and the peak slip of the Mubi fault is located between 2 and 5 km in depth. The slip on the detachment may not be well resolved (also see the checkerboard tests in Fig. S3). Red lines indicate the up-dip edge of each fault, and gray lines indicate the surface-fault traces. The white circle is the epicenter from the U.S. Geological Survey, and the green circle is the centroid location from the Global CMT solution. The blue circle outlines the location of Mount Sisa. The color version of this figure is available only in the electronic edition.

Overall, our model fits the observations well (Fig. 6). However, by comparing individual transects across the Mubi and Mananda faults (Fig. 7) after removing the landslides, our model overestimates uplift near the Mananda fault. Although most of the measurements related to the triggered landslides are excluded in the fault modeling, we suspect that some of them, especially those close to the Mananda fault, may still influence the result of the slip model. Alternatively, this higher misfit in the shallow Mananda fault could be due to the improper assumption of a planar fault geometry in slip



inversions to represent the observed curved fault trace as shown in Figure 3.

DISCUSSIONFault geometry

The results of the subpixel offset suggest that both the Mananda and Mubi faults were involved in the 2018 event, which is more complicated than the single-fault solution proposed in the USGS solution. This two-fault system is also supported by the regional topography, in which one fault trace shown in the subpixel offset follows along the strongly folded belt and another along the imbricate belt (Figs. 1 and 3). Because the USGS epicenter location is in the Mananda fault, we propose that the slip initiated from the Mananda fault, propagated southeastward, and then triggered slip on the Mubi fault. Zhang et al. (2020) perform back-projection imaging using teleseismic data and find slip propagation from northwest to southeast with relatively low-rupture velocities. Although they infer that all of the slip asperities are on the same fault geometry, the southeast propagation of slip is in agreement with our proposed slip process.

Because the Mubi fault is located closer to the New Guinea Highlands, the steeper dip angle fits into a general concept that the fault dip angle gradually increases toward the hinterland (e.g., Fossen, 2016). In fact, a higher amount of horizontal than vertical displacements of the Mananda fault already suggests a shallower dip angle than the Mubi fault (Figs. 6 and 7). This finding is in contrast to the fault geometry proposed by Wang *et al.* (2020), in which they infer a gentler fault dip angle (fault 4

Figure 6. Comparison of observed and modeled surface displacement. The residual is the difference between the observed and modeled displacement. (a—c) horizontal displacement and (d—f) vertical displacement. Red rectangles outline the Mubi fault and the Mananda fault, and the yellow rectangle outlines the detachment. rmse, root mean square error. The color version of this figure is available only in the electronic edition.

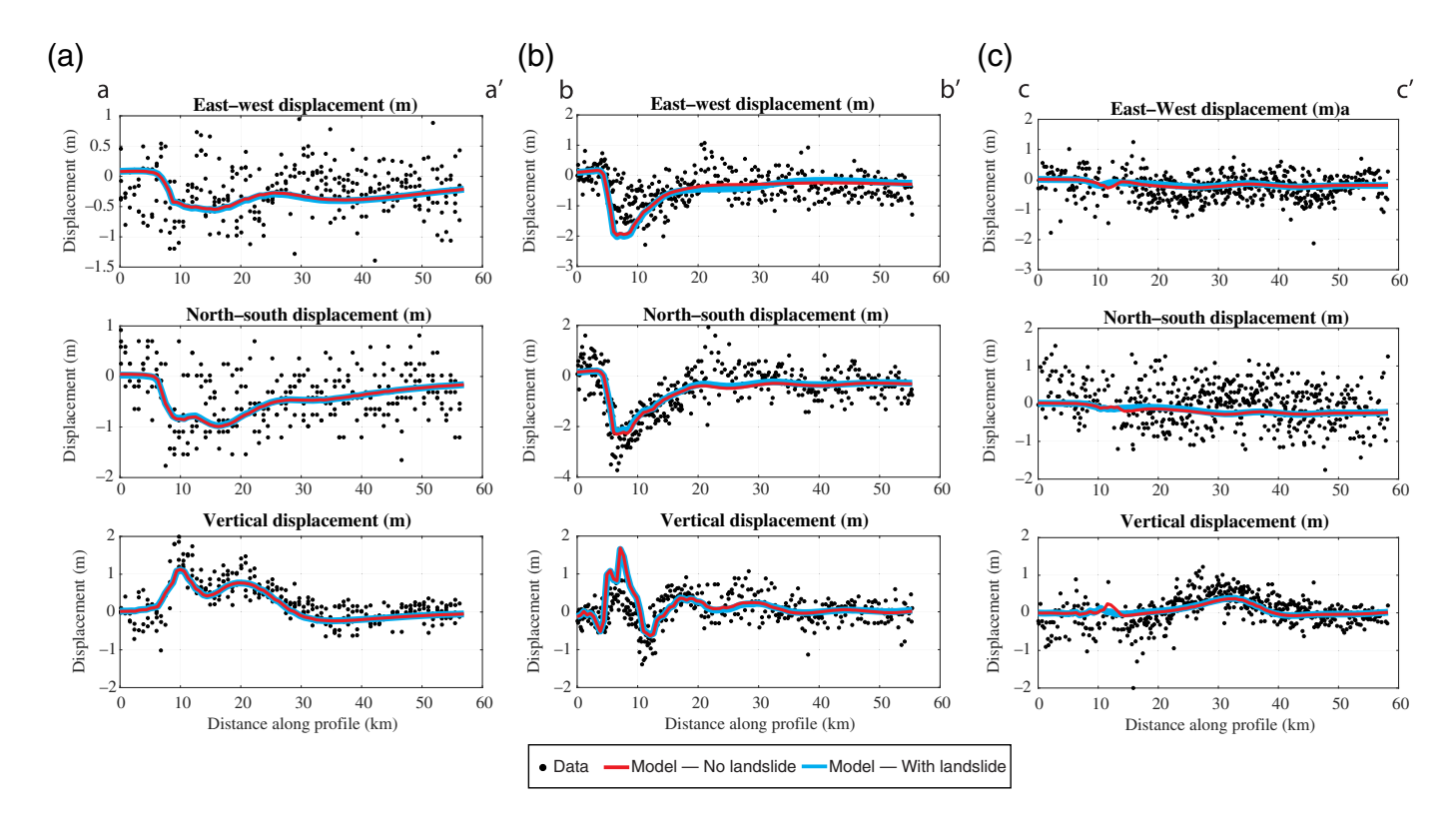
in Wang et al., 2020) toward the hinterland. In addition, we do not find clear evidence of coseismic slip toward the southeast extension of the Mananda fault (fault 3 in Wang et al., 2020).

Because the ascending and descending InSAR cannot well resolve displacement in the north-south direction, we expect a better constrained fault geometry in our study using a full 3D measurement, especially for a fault system that has dominantly north-south and vertical displacements (Fig. 3).

In addition, the ALOS-2 InSAR used in Wang *et al.* (2020) may not reliably resolve coseismic displacement near the faults due to high-phase decorrelation in the near field and phase unwrapping errors (e.g., Fialko *et al.*, 2001). As shown in their slip distribution, there is no shallow slip, which is likely due to lack of measurements in the near field. The subpixel offset results, on the other hand, clearly show more than 1 m of displacement along the Mananda and Mubi fault traces (Figs. 3, 6, and 7), which require shallow slip to predict the displacement (Fig. 5).

Slip distribution on Mananda fault

The subpixel offset result shows a halt of displacement toward the north side of Mount Sisa (north of the Mananda fault trace;



see Fig. 3c). This displacement pattern is also observed in the ALOS-2 InSAR and is explained by a fault geometry with a curved strike (Wang *et al.*, 2020). However, in comparing with the two transects perpendicular to the Mananda fault strike (transects b-b' and c-c' in Fig. 7), the coseismic displacement across the west Mananda fault (transect c-c') is more gradual, implying deeper slip. The relatively simple Mananda fault model proposed in this study can predict the coseismic displacement with deeper slip northeast of Mount Sisa (Fig. 5).

Our fault slip model suggests that there is no shallow slip on the west side of the Mananda fault. The absence of slip can possibly be influenced by the location of Mount Sisa, a dormant volcano that intersects the Mananda fault here (the blue circle in Fig. 5). The increased geothermal gradient below Mount Sisa may have prevented brittle failure (i.e., dynamic rupture) from occurring. Similar observations were found in the 2016 $M_{\rm w}$ 7.1 Kumamoto, Japan, earthquake (e.g., Yagi *et al.*, 2016) in which rupture was terminated by the Aso volcano and the 2017 $M_{\rm w}$ 6.5 Ormoc, Philippines, earthquake in which no coseismic slip was observed below the Tongonan Geothermal Power Plant (Yang *et al.*, 2018).

Coulomb stress analysis and the role of the detachment fault

Stress transfer from an earthquake can trigger seismic and/or aseismic slip in the nearby fault systems laterally or at different depths (Freed, 2005; Hicks and Rietbrock, 2015; Huang *et al.*, 2016; Nissen *et al.*, 2016). Because the Mubi and Mananda faults are not spatially connected, to better understand the stress transfer from the Mananda fault to the detachment

Figure 7. Coseismic displacement across transect (a) a—a' (Mubi fault), (b) b—b' (west of Mananda fault), and (c) c—c' (east of Mananda fault). For each transect, black dots represent the subpixel offset measurements that are less than 6 km away from the transect. Red and blue curves show the predicted displacement from the fault-slip models with and without the removal of landslide subpixel offset measurements, respectively. The color version of this figure is available only in the electronic edition.

and the Mubi fault, we calculate the coulomb stress change using Coulomb 3.3 (Toda *et al.*, 2011). As discussed in the Fault Geometry section, we choose the Mananda fault as the source fault and calculate the static coulomb stress change on the Mubi fault and the detachment.

The coulomb stress transfer (Fig. S4) indicates more than 5 bars (0.5 MPa) of coulomb stress increase on the detachment. As a result, even though slip on the detachment is not well resolved (Fig. S3) due to high measurement uncertainty in the subpixel offset, this amount of coulomb stress increase (>5 bars) may be able to trigger slip on the detachment (Freed, 2005). At this point, whether or not there is slip on the detachment during this event remains inconclusive.

For the Mubi fault, there are up to 5 bars of coulomb stress increase at a 5 km depth. This level of stress increase also suggests slip on the Mubi fault that can be directly triggered by the Mananda fault without the involvement of the detachment. In addition, the USGS epicenter location is on the west side of the Mananda fault, whereas the location of the Global Centroid Moment Tensor (Global CMT) solution (Dziewonski *et al.*, 1981; Ekström *et al.*, 2012) is very close to the peak slip of

our slip model located at the east side of the Mananda fault (Fig. 5). The difference in distance between the USGS epicenter and the Global CMT centroid-location suggests that the event initiated from the west side of the Mananda fault and reached peak slip toward the east side of the Mananda fault. This southeastward slip directivity may significantly increase the dynamic stress change that is not calculated here, and therefore further increase the probability of triggering slip on the Mubi fault (e.g., Wallace *et al.*, 2017).

CONCLUSION

In this study, we use the subpixel offset of the Sentinel-1 SAR images to measure coseismic displacement and conduct finitefault inversions to model fault geometry and slip distribution of the 2018 $M_{\rm w}$ 7.5 Papua New Guinea earthquake. The results show two distinct fault structures, the Mubi fault and the Mananda fault, and a plausible detachment that ruptured during this event. Although there are more than 5 bars of coulomb stress increase on the detachment, slip on the detachment remains inconclusive due to the high measurement uncertainty of the subpixel offset. The termination of shallow slip toward the west side of the Mananda fault could be due to the elevated geothermal gradient in the currently dormant volcano Mount Sisa. For the Mubi fault, both the coulomb stress transfer analysis and the possible southeastward rupture directivity suggest that the slip on the Mubi fault is triggered by the Mananda fault. In addition to fault movement, we also observe earthquake-triggered landslides using the subpixel offset. For earthquakes that generate greater (>1 m) surface displacement, our study demonstrates that the subpixel offset could be a reliable method in mapping fault traces and earthquake-triggered landslides, as well as measuring surface displacement for slip inversions in a densely vegetated and high topographic relief region such as in Papua New Guinea.

DATA AND RESOURCES

We use the U.S. Geological Survey (USGS) National Earthquake Information Center (NEIC) solution for epicenter and aftershock locations at https://earthquake.usgs.gov/earthquakes/eventpage/ us2000d7q6/executive (last accessed August 2018) and https:// earthquake.usgs.gov/earthquakes/search/ (last accessed September 2018). The centroid moment tensor (CMT) is from Global CMT at https://www.globalcmt.org/CMTsearch.html (last accessed June 2020). The Sentinel-1 IW single-look-complex (SLC) data were downloaded from Alaska Satellite Facility (ASF) Vertex at https:// search.asf.alaska.edu/#/ (last accessed August 2018) and processed with using Interferometric Synthetic Aperture Radar (InSAR) Scientific Computing Environment (ISCE; Rosen et al., 2012). In the fault inversion, we used EDGRN/EDCMP code (Wang et al., 2003) to calculate Green's functions based on the Earth's model from the CRUST1.0 model (Laske et al., 2013). All of the subpixel offset results used for inversion can be found in the supplemental material. The optical satellite imagery is the monthly mosaic for March 2018

provided by the Planet Labs, Inc. at www.planet.com (last accessed August 2018). QGIS 3.10 was used to plot Figures 1 and 3 and to remove the landslide displacement. The inset in Figure 1 was acquired from GeoMapApp.

ACKNOWLEDGMENTS

This research is partially supported by Stephen G. Pollock Undergraduate Student Research Grants from the Northeastern Geological Society of America. The authors would like to thank Phil Piccoli for providing valuable comments on the original article. Comments from Associate Editor Ronni Grapenthin, Editor Thomas Pratt, and two anonymous reviewers significantly improved the quality of this article. This work is based on the GEOL 393/394 undergraduate senior thesis project of J.-H. C. at the University of Maryland, College Park. Part of the research is supported by the National Science Foundation (NSF) EAR-2026099 to M.-H. H.

REFERENCES

- Abers, G., and R. McCaffrey (1988). Active deformation in the New Guinea fold-and-thrust belt: Seismological evidence for strike-slip faulting and basement-involved thrusting, *J. Geophys. Res.* **93**, 13,332–13,354, doi: 10.1029/JB093iB11p13332.
- Baldwin, S. L., P. G. Fitzgerald, and L. E. Webb (2012). Tectonics of the New Guinea region, *Annu. Rev. Earth Planet. Sci.* **40**, 495–520, doi: 10.1146/annurev-earth-040809-152540.
- Bekaert, D. P. S., A. Hooper, and T. J. Wright (2015). A spatially variable power law tropospheric correction technique for InSAR data, *J. Geophys. Res.* **120**, 1345–1356, doi: 10.1002/2014JB011558.
- Dziewonski, A. M., T. A. Chou, and J. H. Woodhouse (1981). Determination of earthquake source parameters from waveform data for studies of global and regional seismicity, *J. Geophys. Res.* **86**, 2825–2852, doi: 10.1029/JB086iB04p02825.
- Ekström, G., M. Nettles, and A. M. Dziewonski (2012). The Global CMT Project 2004–2010: Centroid-moment tensors for 13,017 earthquakes, *Phys. Earth Planet. In.* **200/201**, 1–9, doi: 10.1016/j.pepi.2012.04.002.
- Fialko, Y., M. Simons, and D. Agnew (2001). The complete (3-D) surface displacement field in the epicentral area of the 1999 $M_{\rm w}$ 7.1 Hector Mine earthquake, California, from geodetic observations, *Geophys. Res. Lett.* **28**, 3063–3066.
- Fielding, E. J., Z. Liu, O. L. Stephenson, M. Zhong, C. Liang, A. Moore, S.-H. Yun, and M. Simons (2020). Surface deformation related to the 2019 $M_{\rm w}$ 7.1 and 6.4 Ridgecrest earthquakes in California from GPS, SAR interferometry, and SAR pixel offsets, *Seismol. Res. Lett.* 91, 1–12, doi: 10.1785/0220190302.
- Fossen, H. (2016). *Structural Geology*, Cambridge University Press, Cambridge, United Kingdom.
- Freed, A. M. (2005). Earthquake triggering by static, dynamic, and postseismic stress transfer, *Annu. Rev. Earth Planet. Sci.* **33**, 335–367.
- Hamilton, W. (1979). *Tectonics of the Indonesian Region*, U.S. Geological Survey, Professional Papers, 1078.
- Hicks, S. P., and A. Rietbrock (2015). Seismic slip on an upper-plate normal fault during a large subduction megathrust rupture, *Nature Geosci.* **8**, 955–960, doi: 10.1038/NGEO2585.
- Hill, K. C., K. Lucas, and K. Bradley (2010). Structural styles in the Papuan fold belt, Papua New Guinea: Constraints from analog

- modelling, Geol. Soc. Lond. Spec. Publ. **348**, 33–56, doi: 10.1144/SP348.3.
- Huang, M.-H., D. Dreger, R. Bürgmann, S. H. Yoo, and M. Hashimoto (2013). Joint inversion of seismic and geodetic data for the source of the 2010 March 4, 2010 $M_{\rm w}$ 6.3 Jia–Shian, Taiwan, earthquake, *Geophys. J. Int.* **193**, 1608–1626, doi: 10.1093/gji/ggt058.
- Huang, M.-H., E. J. Fielding, H. Dickinson, J. Sun, J. A. Gonzalez-Ortega, A. M. Freed, and R. Bürgmann (2017). Fault geometry inversion and slip distribution of the 2010 $M_{\rm w}$ 7.2 El Mayor-Cucapah earthquake from geodetic data, *J. Geophys. Res.* 122, 607–621, doi: 10.1002/2016 [B012858.
- Huang, M.-H., E. J. Fielding, C. Liang, P. Milillo, D. Bekaert, D. Dreger, and J. Salzer (2017). Coseismic deformation and triggered landslides of the 2016 $M_{\rm w}$ 6.2 Amatrice earthquake in Italy, Geophys. Res. Lett. 44, 1266–1274, doi: 10.1002/2016GL071687.
- Huang, M.-H., H. Tung, E. J. Fielding, H.-H. Huang, C. Liang, C. Huang, and J.-C. Hu (2016). Multiple fault slip triggered above the 2016 $M_{\rm w}$ 6.4 MeiNong earthquake in Taiwan, *Geophys. Res. Lett.* **43**, 7459–7467, doi: 10.1002/2016GL069351.
- Keenan, S. E., and K. C. Hill (2015). The Mananda Anticline, Papua New Guinea: A third oil discovery, appraisal programme and deep potential, *AAPG/SEG International Conf. and Exhibition*, Melbourne, Australia, 13–16 September.
- Kobayashi, T. (2014). Remarkable ground uplift and reverse fault ruptures for the 2013 Bohol earthquake ($M_{\rm w}$ 7.1), Philippines, revealed by SAR pixel offset analysis, *Geosci. Lett.* 1, 7, doi: 10.1186/2196-4092-1-7.
- Koulali, A., P. Tregoning, S. McClusky, R. Stanaway, L. Wallace, and G. Lister (2015). New insights into the present-day kinematics of the central and western Papua New Guinea from GPS, *Geophys. J. Int.* 202, no. 2, 1 August 2015, 993–1004, doi: 10.1093/gji/ggv200.
- Laske, G., G. Masters, Z. Ma, and M. Pasyanos (2013). Update on CRUST1.0—A 1-degree global model of Earth's crust, *Geophys. Res. Abstr.* **15**, 2658.
- Milliner, C., and A. Donnellan (2020). Using daily observations from Planet Labs satellite imagery to separate the surface deformation between the 4 July $M_{\rm w}$ 6.4 foreshock and 5 July $M_{\rm w}$ 7.1 mainshock during the 2019 Ridgecrest earthquake sequence, *Seismol. Res. Lett.* 91, 1986–1997, doi: 10.1785/0220190271.
- Nissen, E., J. R. Elliott, R. A. Sloan, T. J. Craig, G. J. Funning, A. Hutko, B. E. Parsons, and T. J. Wright (2016). Limitations of rupture forecasting exposed by instantaneously triggered earthquake doublet, *Nature Geosci.* 9, 330–336, doi: 10.1038/ngeo2653.
- Pathier, E., E. J. Fielding, T. J. Wright, R. Walker, B. E. Parsons, and S. Hensley (2006). Displacement field and slip distribution of the 2005 Kashmir earthquake from SAR imagery, *Geophys. Res. Lett.* 33, L20310, doi: 10.1029/2006GL027193.

- Rosen, P. A., E. Gurrola, G. F. Sacco, and H. Zebker (2012). The InSAR scientific computing environment, *Proc. of EUSAR*, Nuremberg, Germany, 730–733.
- Toda, S., R. S. Stein, V. Sevilgen, and J. Lin (2011). Coulomb 3.3 graphic-rich deformation and stress-change software for earthquake, tectonic, and volcano research and teaching—User guide, U.S. Geol. Surv. Open-File Rept. 2011-1060, 63 pp., available at http://pubs.usgs.gov/of/2011/1060/ (last accessed March 2020).
- Tregoning, P., H. McQueen, R. Little, and R. Rosa (2000). Present-day crustal motion in Papua New Guinea, *Earth Planets Space* **52**, 727–730, doi: 10.1186/BF03352272.
- Wallace, L. M., Y. Kaneko, S. Hreinsdottir, I. Hamling, Z. Peng, Y. Bartlow, E. D'Anastasio, and B. Fry (2017). Large-scale dynamic triggering of shallow slow slip enhanced by overlying sedimentary wedge, *Nature Geosci.* 10, 765–770, doi: 10.1038/ngeo3021.
- Wallace, L. M., C. Stevens, E. Silver, R. McCaffrey, W. Loratung, S. Hasiata, R. Stanaway, R. Curley, R. Rosa, and J. Taugaloidi (2004). GPS and seismological constraints on active tectonics and arc-continent collision in Papua New Guinea: Implications for mechanics of microplate rotations in a plate boundary zone, J. Geophys. Res. 109, doi: 10.1029/2003JB002481.
- Wang, R., F. L. Martin, and F. Roth (2003). Computation of deformation induced by earthquakes in a multi-layered elastic crust —FORTRAN programs EDGRN/EDCMP, *Comput. Geosci.* 29, 195–207, doi: 10.1016/S0098-3004(02)00111-5.
- Wang, S., C. Xu, Z. Li, Y. Wen, and C. Song (2020). The 2018 $M_{\rm w}$ 7.5 Papua New Guinea earthquake: A possible complex multiple faults failure event with deep-seated reverse faulting, *Earth Space Sci.* 7, e2019EA000966, doi: 10.1029/2019EA000966.
- Yagi, Y., R. Okuwai, B. Enescu, A. Kasahara, A. Miyakawa, and M. Otsubo (2016). Rupture process of the 2016 Kumamoto earthquake in relation to the thermal structure around Aso volcano, *Earth Planets Space* **68**, no. 118, doi: 10.1186/s40623-016-0492-3.
- Yang, Y.-H., M.-C. Tsai, J.-C. Hu, M. A. Aurelio, M. Hashimoto, J. A. P. Escudero, Z. Su, and Q. Chen (2018). Coseismic slip deficit of the 2017 $M_{\rm w}$ 6.5 Ormoc earthquake that occurred along a creeping segment and geothermal field of the Philippine fault. *Geophys. Res. Lett.* **45**, 2659–2668, doi: 10.1002/2017GL076417.
- Zhang, X., W. Feng, H. Du, L. Li, S. Wang, L. Yi, and Y. Wang (2020). The 2018 $M_{\rm w}$ 7.5 Papua New Guinea earthquake: A dissipative and cascading rupture process, *Geophys. Res. Lett.* **47**, e2020GL089271, doi: 10.1029/2020GL089271.

Manuscript received 28 July 2020 Published online 24 November 2020